InGenio Journal
Revista de Ciencias de la Ingeniería de la Universidad Técnica Estatal de Quevedo
https://revistas.uteq.edu.ec/index.php/ingenio
e-ISSN: 2697-3642 - CC BY-NC-SA 4.0

Experimental Study of Defect Detection in Photovoltaic Panels Using Electroluminescence

(Estudio experimental de la detección de defectos en paneles fotovoltaicos utilizando electroluminiscencia)

Franklin Mauricio Gómez López, Danny Vinicio Ochoa-Correa, Isabel Dolores Cabrera Carrera
Universidad de Cuenca, Ecuador.
franklin.gomez@ucuenca.edu.ec, danny.ochoac@ucuenca.edu.ec, isabel.cabrera@ucuenca.edu.ec

Abstract: This study presents an experimental investigation of defect detection in monocrystalline and polycrystalline photovoltaic panels using electroluminescence imaging. Twelve modules with varying levels of degradation, deployed in rural Andean installations, were evaluated through visual inspection and automatic analysis based on convolutional neural networks. The methodology included manual defect segmentation and the application of a U-Net model for automatic classification of structural and electrical anomalies. Results showed that fractures and inactive areas were more frequent in monocrystalline panels, whereas potential-induced degradation (PID) and discoloration were mainly observed in polycrystalline ones. The comparison between manual inspection and the automated model demonstrated high performance in detecting discrete defects such as cracks and busbars, although lower accuracy was obtained for diffuse anomalies like PID. Spatial analysis of defect maps revealed the clustering of certain fault types within cell regions, highlighting the importance of considering spatial correlations in future detection algorithms. These findings support the development of targeted preventive maintenance strategies and reinforce the potential of semantic segmentation as a diagnostic tool for photovoltaic modules.

Keywords: Electroluminescence, photovoltaic panels, preventive maintenance, semantic segmentation, U-Net.

Resumen: Este estudio presenta una investigación experimental sobre la detección de defectos en paneles fotovoltaicos monocristalinos y policristalinos mediante imágenes de electroluminiscencia. Se evaluaron doce módulos con distintos niveles de degradación, instalados en entornos rurales andinos, mediante inspección visual y análisis automático basado en redes neuronales convolucionales. La metodología incluyó la segmentación manual de defectos y la aplicación de un modelo U-Net para la clasificación automática de anomalías estructurales y eléctricas. Los resultados mostraron que las fracturas y áreas inactivas fueron más frecuentes en paneles monocristalinos, mientras que la degradación inducida por potencial (PID) y la decoloración se observaron principalmente en paneles policristalinos. La comparación entre la inspección manual y el modelo automático evidenció un alto desempeño en la detección de defectos discretos como grietas y barras conductoras, aunque con menor precisión en defectos difusos como la PID. El análisis espacial de los mapas de defectos reveló la agrupación de ciertos tipos de fallas dentro de las celdas, destacando la importancia de considerar correlaciones espaciales en futuros algoritmos de detección. Estos hallazgos respaldan el desarrollo de estrategias de mantenimiento preventivo más específicas y refuerzan el potencial de la segmentación semántica como herramienta de diagnóstico para módulos fotovoltaicos.

Palabras clave: Electroluminiscencia, paneles fotovoltaicos, mantenimiento preventivo, segmentación semántica, U-Net.

Recibido (Received): 2025/11/06
Aceptado (Accepted): 2026/04/10

1. INTRODUCTION

The reliability of photovoltaic (PV) installations depends on the integrity of their components, particularly the condition of individual solar cells within the modules. Over time, degradation mechanisms such as micro-cracks, potential-induced degradation (PID), delamination, discoloration, and metallization layer disruptions compromise the energy yield and operational lifespan of PV systems [1], [2], [3]. Beyond their direct impact on energy yield, these defects also reduce the diagnostic signal-to-noise ratio in imaging workflows and complicate large-scale quality assurance as PV deployment accelerates worldwide [4].

Monocrystalline and polycrystalline silicon modules remain the most widely deployed PV technologies, but they differ in structural characteristics and vulnerability to specific defect types [5]. Several comparative studies have reported variations in performance degradation, thermal behavior, and defect propagation across these two material classes [6]. Understanding how defect types manifest and distribute in each case is essential for improving diagnostic accuracy and guiding maintenance strategies. From an operations standpoint, mixed portfolios that combine mono- and multi-Si modules introduce additional variability for condition monitoring systems; models tuned to one substrate may generalize sub-optimally to the other, which motivates explicit, side-by-side analyses of defect prevalence and appearance across materials.

Electroluminescence (EL) imaging has become a common diagnostic technique to inspect defects that are not visible under standard illumination or thermal imaging. When a forward bias is applied to a PV module in darkness, radiative recombination generates infrared emission that can reveal hidden structural and electrical anomalies [7], [8]. The contrast and resolution of EL images, however, depend on capture conditions, the sensitivity of the camera system, and the severity of the defect. Manual interpretation of EL images also introduces subjectivity and may overlook subtle features. Complementary modalities such as infrared (IR) and RGB imaging are increasingly integrated into inspection pipelines at module and plant scale, where IR assists in locating thermally driven anomalies and RGB highlights surface-level issues like broken glass, discoloration, or delamination, enabling faster triage in field campaigns [4].

In recent years, machine learning approaches, particularly convolutional neural networks (CNNs), have been employed to support automatic defect segmentation and classification. Among these, the U-Net architecture has been applied to PV inspection tasks using electroluminescence imaging, showing encouraging performance in pixel-level detection [9], [10], [11]. Despite these advancements, few studies have examined whether model performance or defect detection outcomes vary when applied to different module types. A systematic comparison between monocrystalline and polycrystalline panels-using both visual and automated inspection methods-remains limited in current literature.

Recent surveys emphasize a shift from handcrafted feature pipelines toward end-to-end CNNs for EL image analysis, while underscoring persistent challenges: defect diversity, scale variation, class imbalance, and domain shifts between laboratory and field data [12].

To mitigate data scarcity, synthetic EL datasets produced with deep convolutional generative adversarial networks (DCGANs) have been introduced, reaching quality indicators (e.g., Inception Score and FID) that support their use to augment training sets and to probe the relationship between image patterns and electrical performance via learned regressors [13].

At the detector level, one-stage architectures (e.g., YOLOv5) combined with tailored loss functions—such as focal and efficient IoU (EIoU) variants—have shown gains in mean average precision for multi-class EL defect detection, particularly under class imbalance and scale heterogeneity [14].

This study presents an experimental evaluation of defect detection in monocrystalline and polycrystalline PV panels using EL imaging. Manual and U-Net-based inspections are performed on a shared dataset, enabling a comparative assessment of defect type prevalence, spatial distribution, and detection accuracy across material types. The work also analyzes how common degradation modes manifest differently in each case, contributing to the development of more targeted inspection and maintenance protocols for silicon-based PV modules.

2. MATERIALS AND METHODS

2.1. Panel samples and degradation overview

The experimental study was conducted on a set of 12 PV panels, including six monocrystalline and six polycrystalline modules, representative of systems deployed in rural Andean installations. Technical specifications of the modules are presented in Table 1. All panels exhibited varying degrees of physical and electrical degradation, with service durations ranging from 5 to 10 years under typical field conditions. Experimental evaluations were conducted at the Microgrid Laboratory of the University of Cuenca, Ecuador [15].

Table 1. Specifications of tested PV modules.

Type	Model	P_{max}(W)	Service(yrs)
Monocrystalline	Heckert NeMo 60 P260	260	7
Polycrystalline	Canadian Solar CS6P-250P	250	8

Visual inspections and EL imaging revealed a wide range of degradation patterns, classified according to IEC 61215 [16]. Observed modes included interconnect ribbon corrosion, solder bond failure, cell cracks, PID, busbar interruptions, and discoloration due to encapsulant browning.

Figure 1 illustrates the representative degradation patterns found in the samples. Figure 1(a) shows severe encapsulant discoloration (browning) concentrated in the active cell areas, a typical sign of chemical degradation due to UV exposure. Figure 1(b) highlights external factors such as accumulated dust along the frames and localized bird droppings, which induce partial shading. Additionally, Figure 1(c) reveals oxidation. It is important to note that while these defects were identifiable through visual inspection, structural fractures and microcracks remained invisible to the naked eye, necessitating the subsequent use of electroluminescence imaging for their detection.

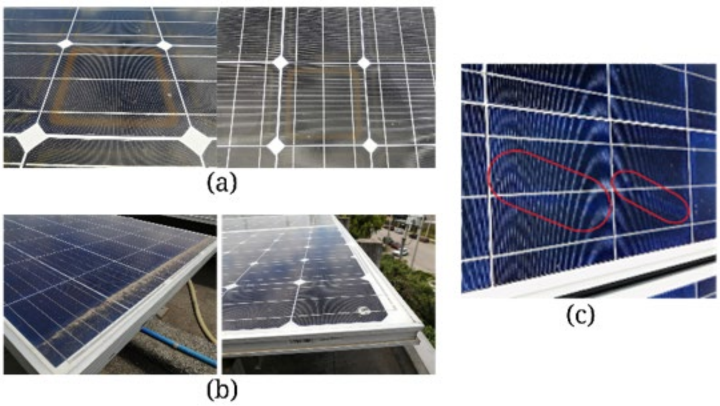

Figure 1. Visible degradation observed during physical inspection: (a) Encapsulant discoloration (browning) in the center of the cells; (b) Soiling accumulation and bird droppings on the glass surface; (c) Signs of corrosion.

2.2. Image acquisition and experimental setup

The EL image acquisition process was conducted in a darkroom to minimize ambient interference. Each module was forward-biased using a programmable Chroma DC power supply to induce electroluminescence, with polarization currents set to approximately 6 A (two-thirds of I_{SC}). The camera used was an OWL 640 M model equipped with an InGaAs sensor, sensitive to the 900–1700 nm wavelength range.

Images were captured using the XCAP-Std software with the following configuration: exposure time between 30–50 ms, digital gain factor of 2.5, and three-point non-uniformity correction (offset, gain, dark). Figure 2 shows the laboratory setup used during the inspection process.

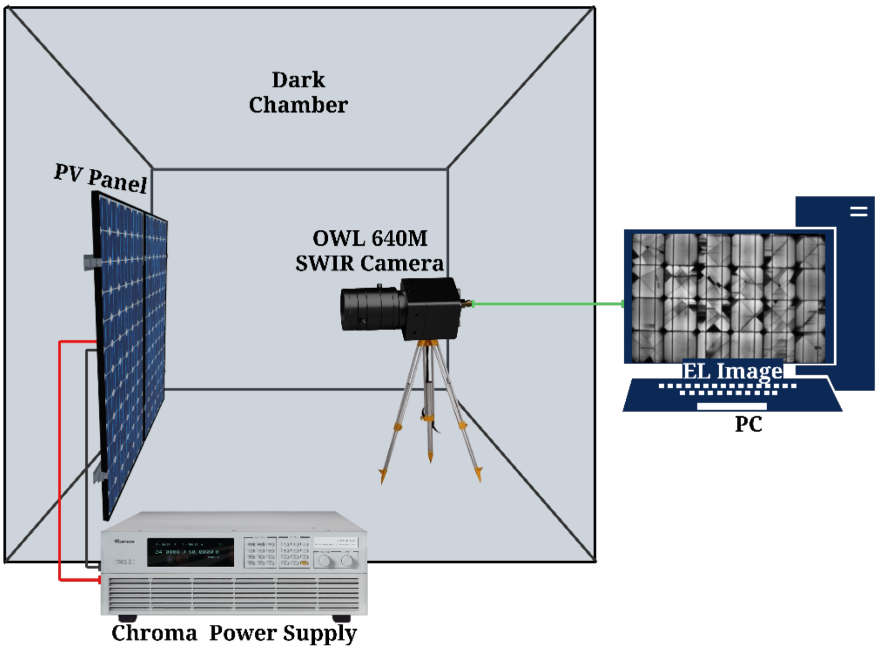

Figure 2. Experimental setup showing the EL imaging system in the darkroom environment.

2.3. Ground Truth generation via visual inspection

To establish a reliable reference for supervised learning, a rigorous visual inspection was conducted solely to generate the Ground Truth dataset. Each EL image was segmented into individual cells and independently evaluated by three expert reviewers. The classification process labeled four main defect categories: cell breaks (visible micro-cracks disrupting current flow), PID (darker areas with reduced luminescence), discoloration (localized dimming due to aging), and finger interruptions (breaks in metallization lines). The manual annotations were recorded and cross-validated among reviewers to create the final target masks used for training and evaluating the automated system.

2.4. U-Net based semantic segmentation

Automatic defect detection was implemented using a U-Net architecture, trained on the annotated dataset derived from the visual inspection phase. The input consisted of preprocessed EL images, standardized in resolution and contrast.

The network consisted of four encoder-decoder levels, using ReLU activation and dropout layers for regularization. The dataset was split into 70% training, 15% validation, and 15% testing. The training outcomes, including F1 score, recall, and precision, are summarized in Table 2, which presents the performance metrics obtained for the optimized U-Net_V32 model.

Table 2. Training performance of U-Net_V32.

Model Version	F1 Score	Recall	Precision
U-Net_V32	0.9064	0.9066	0.8714

2.5. Implementation details and reproducibility

The U-Net models were implemented using the PyTorch framework (v2.3.1). Training and inference procedures were executed on the Google Colab Pro platform, utilizing an NVIDIA T4 GPU with 16 GB of VRAM. The input EL images were resized to 256×256 pixels using bilinear interpolation to preserve spatial details, while nearest-neighbor interpolation was applied to the ground truth masks to maintain class integrity.

The training process employed the Adam optimizer with an initial learning rate of 0.0018 and a batch size of 16 samples. A cross-entropy loss function was minimized over 48 epochs, with a step-based learning rate decay (factor of 0.05 every 8 epochs) to facilitate convergence. Under this configuration, the average inference time was approximately 32 ms per image, demonstrating the model's feasibility for high-throughput processing in industrial scenarios.

2.6. Evaluation metrics

Model performance was evaluated using pixel-based accuracy, Dice score, and class-level recall. These metrics were computed for each defect category on mono and polycrystalline modules independently. Statistical comparison between module types was conducted using paired t-tests to assess differences in segmentation accuracy.

Defect frequency maps and classification heatmaps were also generated to visualize spatial distribution, as discussed further in the next section.

3. RESULTS

3.1. Defect frequency and type distribution

A total of 142 cells were evaluated through visual inspection using EL imagery. The breakdown of defect types across three tested PV modules is presented in Table 3. The most frequently detected issues were material anomalies and conductor finger interruptions. The presence of PID was exclusive to polycrystalline modules, while contact interruptions were absent in monocrystalline samples.

Table 3. Visually identified defects per module.

Module Type	Material Anomalies	Contact Interruptions	Finger Interruptions	PID
Monocrystalline	11 cells	0	24 cells	18
Polycrystalline 1	25 cells	11 cells	0	14
Polycrystalline 2	25 cells	11 cells	0	11

3.2. Automatic detection results

The segmentation model was trained to identify three categories—conductor bars, cracks, and inactive dark zones—using expert-generated Ground Truth masks as the reference for supervised learning and evaluation. Table 4 presents a clear, class-by-class quantitative comparison of the U-Net_V32 performance using precision, recall, and F1-score. In particular, the final model (U-Net_V32) achieved an F1-score of 0.9083 for conductor bar detection, 0.6557 for crack identification, and 0.6466 for inactive-zone segmentation. In addition to these aggregated metrics, Figure 4 provides a qualitative, pixel-level comparison between the Ground Truth masks and the U-Net_V32 predictions, including error maps that distinguish false positives (FP) and false negatives (FN), thereby highlighting where the model agrees with the manual annotations and where discrepancies occur.

Table 4. Performance metrics for U-Net_V32.

Defect Category	Precision	Recall	F1 Score
Conductor Bars	0.9151	0.9031	0.9083
Cracks	0.6794	0.6465	0.6557
Inactive Zones	0.6643	0.6443	0.6466

3.3. Spatial patterns of defects

Figure 3 illustrates three distinct heatmaps showing the spatial distribution of predictions for busbars, cracks, and dark zones on monocrystalline modules. The heatmap for busbars demonstrates their consistent and localized presence within the module. In contrast, the heatmaps for cracks and dark zones reveal that these defects had a higher occurrence in the central regions of the cells. The co-occurrence matrix, shown in Figure 4, highlights the conditional presence of multiple defect types in the same cell regions.

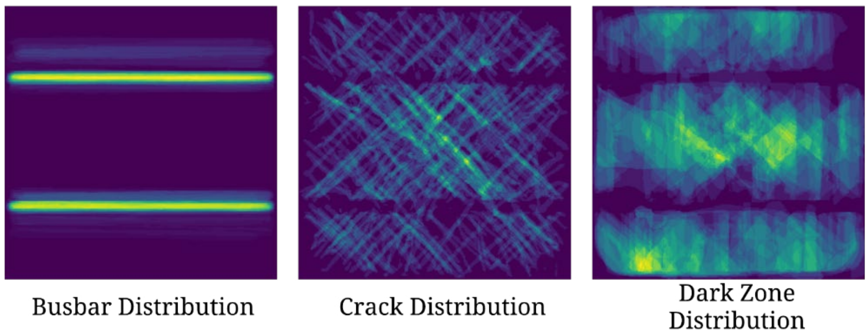

Figure 3. Heatmaps showing defect distribution across cells in monocrystalline module.

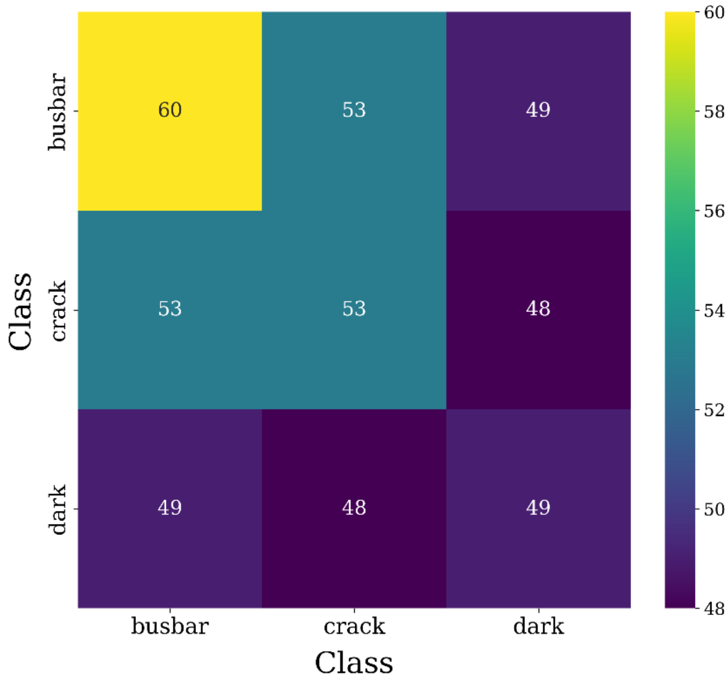

Figure 4. Co-occurrence matrix of defects in monocrystalline cells.

3.4. Case studies

To assess model accuracy at the image level, a representative cell was manually annotated and its predicted segmentations were compared. Figure 5 shows a visual comparison of U-Net_V32 predictions against manual annotations for the cracks, dark zones, and busbar defects within this single cell. The figure also includes error maps, highlighting false positives and false negatives for each defect type. The U-Net_V32 model demonstrated proficiency in identifying microcracks not marked by the manual classifier, suggesting that EL signal attenuation can be captured algorithmically even when visually imperceptible. However, it occasionally misclassified encapsulant delamination artifacts as inactive zones.

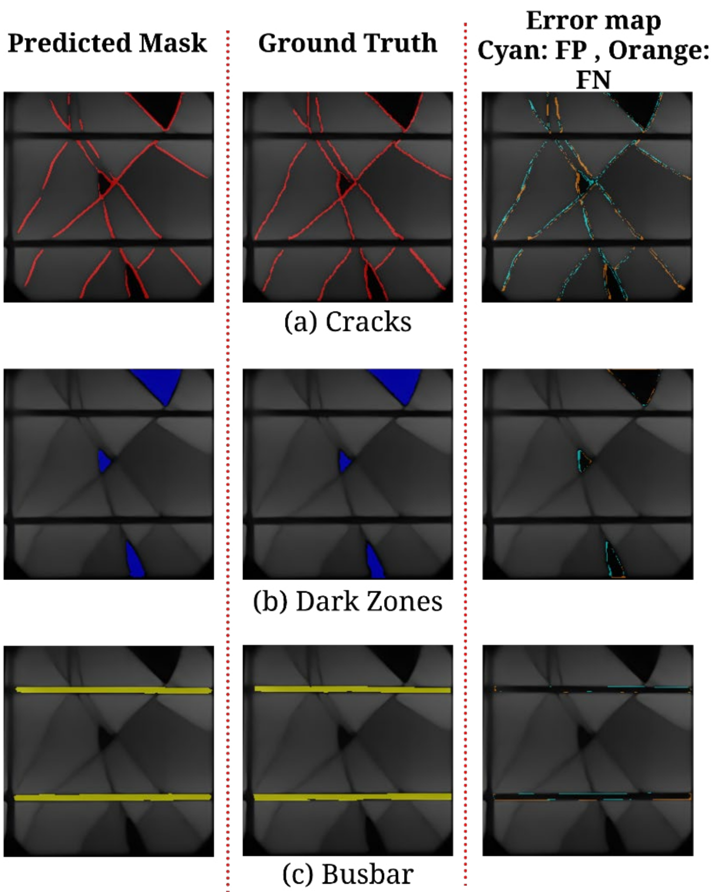

Figure 5. Qualitative comparison of segmentation performance. Each row corresponds to a specific defect class: (a) Cracks, (b) Dark Zones, and (c) Busbars. The columns display the U-Net prediction, the Ground Truth (manual annotation), and the spatial Error Map. In the error maps, Cyan pixels represent False Positives (over-segmentation), while Orange pixels indicate False Negatives (missed defects).

4. DISCUSSION

The results provide multiple layers of interpretation regarding the classification of defects in PV modules through EL imaging. One of the central observations is the disparity in defect prevalence between mono- and polycrystalline modules. Although both types exhibited broken cells, inactive regions, and discoloration, fractures were especially concentrated in monocrystalline samples. This trend is consistent with the higher structural uniformity of mono-Si wafers, which tend to propagate mechanical stress more efficiently. Conversely, PID and snail trails were more commonly detected in polycrystalline modules, indicating distinct degradation pathways influenced by material properties and manufacturing conditions.

The defect maps and co-occurrence matrices reinforce these findings. As shown in Figure 3, defects such as cracks and dark zones appeared concurrently in multiple cells, suggesting spatial clustering. In mono modules, 48 cells were simultaneously marked with cracks and inactive areas. These results emphasize the importance of including spatial correlation when developing defect detection algorithms, particularly for defect classes that emerge in proximity.

The automatic segmentation achieved through U-Net produced consistent predictions across several categories, with high F1 scores for crack detection and busbar alignment. However, performance varied by defect type. For example, the identification of PID was less accurate, possibly due to its diffuse appearance and lower contrast under EL. These outcomes align with findings from previous studies that highlight the difficulties of detecting uniform degradation patterns compared to discrete faults such as fractures or inactive zones.

Compared with prior EL-based inspection studies that focus primarily on reporting segmentation accuracy, the present work adds three practical elements that become relevant under real field conditions. First, the dataset is built from mono- and polycrystalline modules with degradation accumulated in service (rather than controlled laboratory aging), which exposes the model to realistic variability in soiling, corrosion, and encapsulant discoloration that can interfere with EL interpretation. Second, the Ground Truth was generated through cross-validated expert annotations, and the evaluation is explicitly anchored to a pixel-level comparison (including FP/FN error maps), enabling a more transparent identification of failure modes rather than relying only on aggregate scores. Third, beyond per-class metrics, the study analyzes the spatial organization of defects (co-occurrence and clustering), showing that cracks and inactive regions often appear jointly within neighboring cells; information that can be integrated into inspection workflows to prioritize modules or strings for targeted maintenance and further testing.

When comparing manual and automatic assessments, qualitative agreement was observed in most annotated panels. Nonetheless, certain cases showed undersegmentation by the model, especially for defects located at the edges or overlapping with frame artifacts. These discrepancies underline the importance of training with representative samples that include peripheral and partially obscured defects.

Limitations in the current implementation stem from the relatively small annotated dataset and the fixed architecture of the segmentation model. Although the version trained (U-Net_V32) was optimized with adjusted filters and skip connections, future work should examine ensemble strategies or hybrid approaches that merge multiple model outputs. Additionally, data augmentation strategies could be enhanced to simulate edge-based distortions and noise patterns encountered in real field conditions.

5. CONCLUSIONS

This study evaluated the detection of structural and electrical defects in mono- and polycrystalline PV panels through EL imaging combined with U-Net-based semantic segmentation. A comparative analysis revealed that fractures and inactive areas were more frequent in monocrystalline modules, whereas PID and surface discoloration appeared predominantly in polycrystalline ones.

Manual inspection protocols were cross-validated with automated segmentation outputs. Using expert-generated Ground Truth masks as the reference, the final U-Net version (U-Net_V32) provided a clear class-by-class performance, achieving an F1-score of 0.9083 for conductor bar (busbar) detection, 0.6557 for crack identification, and 0.6466 for inactive-zone segmentation. The model achieved strong F1 performance on discrete defects such as cracks and disconnected busbars, but underperformed in detecting diffuse anomalies like PID. This indicates that CNN-based segmentation can support diagnostic assessments, provided that training datasets cover sufficient variation in defect morphology and imaging artifacts.

The spatial distribution analysis confirmed that certain defects appear in clusters, especially in mono panels, highlighting the relevance of incorporating spatial information into diagnostic workflows. Although the model correctly classified most defect types, limitations remain in handling image boundaries and overlapping noise patterns. In practical terms, these results support the use of EL-driven segmentation as a screening tool to prioritize modules for further inspection, while emphasizing that improved labeling diversity and artifact-aware training are needed to increase reliability for low-contrast and diffuse degradation signatures (e.g., PID).

The findings of this study also emphasize the industrial applicability of EL-based segmentation for enhancing preventive maintenance strategies in photovoltaic systems. The model's ability to prioritize modules for inspection based on defect severity offers significant potential for optimizing maintenance schedules and reducing operational downtime in large-scale PV installations.

In terms of scalability, the methodology can be expanded to handle larger datasets by leveraging batch processing and incremental model training, ensuring that it remains feasible for wide-scale deployment in the industry. Additionally, this framework can be adapted to different PV technologies and expanded to include additional defect categories.

Future work should focus on extending the training dataset, improving edge-specific augmentation strategies, and integrating temporal EL imaging for defect tracking. Further improvements in the training process could include hybrid and ensemble approaches, as well as better artifact handling through more diverse and realistic training data. Overall, the methodology supports a structured framework for comparing degradation patterns across different PV technologies and contributes to enhancing inspection strategies for preventive maintenance.

ACKNOWLEDGMENTS: The authors thank Universidad de Cuenca for easing access to the facilities of the Microgrid Laboratory of the Faculty of Engineering, for allowing the use of its equipment, and for authorizing its staff the provision of technical support necessary to carry out the experiments described in this article.

REFERENCES

[1] R. Zhang *et al.*, “Optimizing PV Panel Segmentation in Complex Environments Using Pre-Training and Simulated Annealing Algorithm: The JSWPVI”, *Land*, vol. 14, no. 6, jun. 2025. [Online]. Available: https://doi.org/10.3390/land14061245

[2] H. Munawer Al-Otum, “Deep learning-based automated defect classification in Electroluminescence images of solar panels”, *Adv. Eng. Inform*, vol. 58, oct. 2023. [Online]. Available: https://doi.org/10.1016/j.aei.2023.102147

[3] A. El-Tayeb, F. Li, A. Kumar, y G. Tamizhmani, “Electrical Impedance Spectroscopy: A Complementary Approach Differentiating PID Mechanisms in Photovoltaics”, *Electronics*, vol. 14, no. 5, pp. 1021, mar. 2025. [Online]. Available: https://doi.org/10.3390/electronics14051021

[4] D. Matusz-Kalász, I. Bodnár, y M. Jobbágy, “An Overview of CNN-Based Image Analysis in Solar Cells, Photovoltaic Modules, and Power Plants”, *Appl. Sci.*, vol. 15, no. 10, pp. 5511, jan. 2025. [Online]. Available: https://doi.org/10.3390/app15105511

[5] A. Tihane, M. Boulaid, A. Elfanaoui, M. Nya, y A. Ihlal, “Performance analysis of mono and poly-crystalline silicon photovoltaic modules under Agadir climatic conditions in

Morocco", *Mater. Today Proc.*, vol. 24, pp. 85-90, jan. 2020. [Online]. Available: https://doi.org/10.1016/j.matpr.2019.07.620

[6] M. Köntges, S. Kurtz, C. Packard, U. Jahn, K. A. Berger, y K. Kato, *Performance and reliability of photovoltaic systems: subtask 3.2: Review of failures of photovoltaic modules: IEA PVPS task 13: external final report IEA-PVPS*. Sankt Ursen: International Energy Agency, Photovoltaic Power Systems Programme, 2014. [Online]. Available: https://doi.org/10.2314/GBV:856979287

[7] T. Fuyuki, H. Kondo, T. Yamazaki, Y. Takahashi, y Y. Uraoka, "Photographic surveying of minority carrier diffusion length in polycrystalline silicon solar cells by electroluminescence", *Appl. Phys. Lett.*, vol. 86, no. 26, pp. 262108, jun. 2005. [Online]. Available: https://doi.org/10.1063/1.1978979

[8] Y. Zhang, R. Wang, F. Wang, D. Zhu, X. Gong, y X. Cheng, "Electroluminescence as a Tool to Study the Polarization Characteristics and Generation Mechanism in Silicon PV Panels", *Appl. Sci.*, vol. 13, no. 3, pp. 1591, 2023. [Online]. Available: https://doi.org/10.3390/app13031591

[9] R. A. M. Rudro *et al.*, "SPF-Net: Solar panel fault detection using U-Net based deep learning image classification", *Energy Rep.*, vol. 12, pp. 1580-1594, dic. 2024. [Online]. Available: https://doi.org/10.1016/j.egyr.2024.07.044

[10] F. Gómez-López, D. Ochoa-Correa, y I. Cabrera-Carrera, "U-Net–based semantic segmentation of defects in photovoltaic panels", *Ingenius*, no. 35, pp. 110-121, jan. 2026. [Online]. Available: https://doi.org/10.17163/ings.n35.2026.08

[11] A. B. Alao, O. M. Adeyanju, M. Chamana, S. Bayne, y A. Bilbao, "Photovoltaic Farm Power Generation Forecast Using Photovoltaic Battery Model with Machine Learning Capabilities", *Solar*, vol. 5, no. 2, p. 26, 2025. [Online]. Available: https://doi.org/10.3390/solar5020026

[12] T. Hussain, M. Hussain, H. Al-Aqrabi, T. Alsboui, y R. Hill, "A Review on Defect Detection of Electroluminescence-Based Photovoltaic Cell Surface Images Using Computer Vision", *Energies*, vol. 16, no. 10, pp. 4012, ene. 2023. [Online]. Available: https://doi.org/10.3390/en16104012

[13] H. F. M. Romero *et al.*, "Synthetic Dataset of Electroluminescence Images of Photovoltaic Cells by Deep Convolutional Generative Adversarial Networks", *Sustainability*, vol. 15, no. 9, jan. 2023. [Online]. Available: https://doi.org/10.3390/su15097175

[14] S. Ding, W. Jing, H. Chen, y C. Chen, "Yolo Based Defects Detection Algorithm for EL in PV Modules with Focal and Efficient IoU Loss", *Appl. Sci.*, vol. 14, no. 17, pp. 7493, jan. 2024. [Online]. Available: https://doi.org/10.3390/app14177493

[15] J. L. Espinoza, L. G. González, y R. Sempértegui, "Micro Grid Laboratory as a Tool for Research on Non-Conventional Energy Sources in Ecuador", en *2017 IEEE International Autumn Meeting on Power, Electronics and Computing (ROPEC)*, 2017, pp. 1-7. [Online]. Available: https://doi.org/10.1109/ROPEC.2017.8261615

[16] International Electrotechnical Commission, "IEC 61215-1:2016 - Terrestrial Photovoltaic (PV) Modules – Design Qualification and Type Approval – Part 1: Test Requirements". 2016. [Online]. Available: https://www.iecee.org/certification/iec-standards/iec-61215-12021